# Phase Transition Enhanced Pyroelectric Nanogenerators for Self-Powered Temperature Sensors

Hongyu Li[1,3], Chris R. Bowen[2], and Ya Yang[1,3,4*]

[1]*CAS Center for Excellence in Nanoscience, Beijing Key Laboratory of Micro-nano Energy and Sensor, Beijing Institute of Nanoenergy and Nanosystems, Chinese Academy of Sciences, Beijing 101400, P. R. China.*

[2]*Department of Mechanical Engineering, University of Bath, BA27AK, UK*

[3]*School of Nanoscience and Technology, University of Chinese Academy of Sciences, Beijing, 100049, China.*

[4]*Center on Nanoenergy Research, School of Physical Science and Technology, Guangxi University, Nanning 530004, PR China.*

*Corresponding author. Email: yayang@binn.cas.cn (Y. Yang).

**ABSTRACT:** Pyroelectric materials are of interest for waste heat utilization and thermal detection. However, the low output current and inefficiency reduces their effectiveness. Here, we utilize the abrupt decrease in polarization of ferroelectric $BaTiO_3$ materials around Curie temperature to improve the output performance of a pyroelectric nanogenerator. The variation of the polarization leads to a large change in the density of surface free charges, resulting in an increase of pyroelectric current. We have designed a temperature control and recording system to realize direct measurement of the pyroelectric output current. The pyroelectric current, power and energy conversion efficiency of the device near the Curie temperature were measured to be 15.6-fold, 18-fold and 15.8-fold higher than those acquired near room temperature. Moreover, the temperature induced current and charge density enhancement can be applied to detect temperature and temperature change. The responsivity of the self-powered temperature sensor near $T_c$ is 120 $nC/cm^2 \cdot K$, which 4.8 times higher than that near room temperature (25.1 $nC/cm^2 \cdot K$). The results confirmed the ability to exploit a ferroelectric phase transition for pyroelectric performance enhancement.

**KEYWORDS:** ferroelectric, pyroelectric, phase transition, $BaTiO_3$

# 1. INTRODUCTION

With the demands for clean energy and low-power portable electronics, the drive to develop new renewable energy sources for self-powered sensors is attracting growing interest.[1-10] The ability to harvest low-grade waste heat is of particular concern since, according to the data from the U. S. Department of Energy, a significant amount of waste heat from our daily life and core industries, such as, iron/steel, paper, glass, cement, aluminum, and chemical production is lost every day.[11] While new approaches to utilize waste heat can provide new forms of green energy to reduce pollution and carbon emissions, scavenging heat can also be applied to provide self-powered sensor systems for smart portable electronics and sensor networks. Thermoelectric materials have attracted interest since they able to generate electrical energy from a *spatial* temperature gradients ($dT/dx$), where a number of semiconductors and conductive polymers exhibit thermoelectric properties.[12-15] As an alternative approach, pyroelectric materials are polar dielectric materials with a non-centrosymmetric structure that can convert temperature fluctuations ($dT/dt$) into electric energy as a result of a change in polarization with temperature.[16-19]

Pyroelectric nanogenerators have been considered for thermal energy harvesting and temperature detection; these include infrared and person detection, thermal imaging, electronic skins, and wearable health monitoring devices.[20-26] While the voltage generated by the pyroelectric effect can be relatively high, the current is often relatively low, which ultimately limits the output power. In addition, the low energy conversion efficiency and the naturally low frequency of thermal cycles impedes the application of pyroelectric materials to thermal harvesting. Several methods have been applied to improve the performance of pyroelectric materials; these include electric field enhancement, grain size control and device thickness control.[27, 28] Pandya *et al.* reported on the electric field enhanced

pyroelectric performance of a $0.68Pb(Mg_{1/3}Nb_{2/3})O_3$-$0.32PbTiO_3$ ferroelectric, the pyroelectric coefficient was enhanced from 100 μC/m$^2$·K to 550 μC/m$^2$·K, and the dielectric constant was suppressed by 72% by the application of a DC electric field.[29] Patel *et al.* observed that the grain size influenced the pyroelectric performance of $BaTiO_3$ based ceramics. On increasing the grain size from 136 nm to 529 nm the pyroelectric coefficient and performance figures of merit exhibited a five-fold increase. As a result, the energy generated using a Olsen cycle was enhanced from ~96 kJ/m$^3$ to ~135 kJ/m$^3$.[30] Song *et al.* studied the dimensional control of a pyroelectric element, whereby a thin free-standing indium tin oxide (ITO)/$BaTiO_3$ /Ag pyroelectric nanogenerator exhibited a pyroelectric charge density that was 11.4 times higher than that of thick device which was attached on a substrate.[16] Yang *et al.* reported a single $PbZrTiO_3$ micro/nano wire based pyroelectric self-powered temperature sensor which can detect both temperature and the change rate of temperature of the heat source. The reported temperature sensor possessed a short response time of 0.9 s and a good sensitivity of 0.4 K.[31]

The pyroelectric coefficient, $p$, is defined by

$$p = \frac{\mathrm{d}P_s}{\mathrm{d}T} \tag{1}$$

where $T$ represents temperature, $p$ is the pyroelectric coefficient and $P_s$ is the spontaneous polarization. According to the literature, the rate of change of the spontaneous polarization with temperature ($dP_s/dT$) is increases significant near its phase transition temperature at the Curie temperature ($T_c$) .[6] As a result, the pyroelectric coefficient can be improved near the $T_c$, such as a ferroelectric-antiferroelectric transition, or a ferroelectric-paraelectric transition. Sun *et al.* reported on a molecular pyroelectric material which exhibited an improvement is performance near its transition temperature[32], where $AgNO_3$ based ceramics were confirmed to exhibit an outstanding pyroelectric energy density of 1.4

J/cm$^3$ at an antiferroelectric-ferroelectric phase boundary.[33]

In this work, we have studied the temperature-dependent pyroelectric behavior of $BaTiO_3$ (BTO) ceramics. BTO has been selected as an environmentally friendly and lead-free ferroelectric material with excellent pyroelectric performance, where the ferroelectric-paraelectric phase transition temperature (Curie temperature, $T_c$) is ~ 130 °C.[34] In previous work, the temperature dependence of pyroelectric coefficient of BTO based materials was obtained by *P-E* loops or thermally stimulated depolarization current.[30, 35-37] The pyroelectric output current and power at a wide temperature range were measured for the first time in this work. The BTO ceramics were obtained by two-step sintering method[38] and to assess the pyroelectric properties, the ambient temperature during the measurement process was controlled by a sealed thermostat and the pyroelectric current as a result of a temperature change was measured from room temperature (below $T_c$) to 140 °C (above $T_c$). Notably, the pyroelectric current near $T_c$ was found to be 15.6 times higher than that near room temperature and the performance figures of merit were enhanced by at least 3.5 times. Moreover, the pyroelectric device can sense temperature by output current and temperature change by charge density change. The responsivity of the temperature sensor was also enhanced by 4.8 times near $T_c$. The results indicate the potential of exploiting the pyroelectric response near its phase transition temperature for enhancement of pyroelectric performance.

## 2. EXPERIMENTAL SECTION

**Preparation of $BaTiO_3$ ceramic and Ag/BTO/Ag device.** The BTO ceramic was fabricated using commercial BTO nanopowders. (Aladdin industrial Corporation). A mass of 0.3 g of BTO powder was mixed with a polyvinyl alcohol (2 wt%) binder uniformly. Then, the mixed sample was pressed into a disk with a diameter of 10 mm under a 2 MPa pressure and pressed by cold isostatic

pressing under 250 MPa. Next, the pressed sample was placed in an alumina crucible and sintered by a two-step sintering method. Firstly, the sample was heated to 650 ºC and held at the temperature for 1h to remove the binder. Secondly, the temperature was increased to 1150 ºC and rapidly reduced to 900 ºC. Finally, the sample was maintained at 900 ºC for 20 h to densify the material. Then, the densified BTO ceramic was polished and a disk with a thickness of 0.7 mm was obtained. Ag electrodes were sputtered on the upper and lower planes of the BTO ceramic disk. The Ag/BTO/Ag device was poled at an electric field of 3 kV/mm at room temperature for 30 minutes in silicone oil (Nanjing Entai Electronic Instruments Plant, ET2673D-4 Piezoelectric Ceramics High-voltage Poling Device).

**Characterization and Measurements.** A cross section image of the BTO ceramic was analyzed by scanning electron microscopy (Nova NanoSEM 450). Phase transitions of the BTO ceramic was investigated by a differential scanning calorimeter (volumetric specific heat capacity) (Hengjiu HSC-1) and dielectric temperature spectrometer (temperature-dependent permittivity via a Partulab DMS500). A Peltier cooling plate was used to provide temperature fluctuations. A thermocouple (OMEGA) and multichannel temperature recorder (Jinke JK4008) was used to measure and record the temperature with time. The pyroelectric current was recorded by a digital source meter (Keythley 2611B) and polarisation-electric field (*P-E)* loops were investigated by ferroelectric measurement system (Radiant RTI-MultiFerroic).

## 3. RESULTS AND DISCUSSION

The selected bulk material for a pyroelectric generator should possess a phase transition at a relevant and useful temperature range relative to the temperature source being harvested. In this regard, the BTO ceramics exhibit a bistable phase transition at ~130 ºC, which accompanied by the decrease

of the spontaneous polarization. A two-step sintering method was applied to obtain BTO ceramics with a clear ferroelectric-paraelectric phase transition and a reduced peak permittivity. To investigate the pyroelectric performance at a range of temperatures, there was a need to develop temperature fluctuations at a range of ambient temperatures; this was achieved using a temperature adjustable thermostat combined with a temperature control plate.

To produce BTO ferroelectric ceramics via the two-step sintering method, the pressed power specimen was initially heated to 1150 ºC and the temperature was rapidly reduced to 900 ºC and maintained for 20 hours. During the two-step sintering process, the sample is heated to a higher temperature to achieve a medium density at the first step. The inter-particle pores get a critical size during this process. Then, the temperature dramatically decreases to a lower temperature which can drive the pores further shrink but not enough to drive the grain growth at the second step.[39] In this work, the BTO sample was heated to 1150 ºC to get a medium density and grain growth. Then the temperature rapidly decreased to 900 ºC to eliminated the pores without grain size increasing. Thus, the specimen was densified at a low temperature without significant grain growth, where the sintered ceramic exhibited a grain size of several hundred nanometer; see Fig. S1. The temperature-dependent pyroelectric characteristics of the BTO ceramic was investigated using a thermostat whose temperature ($T$) could be accurately controlled through software. A front and side schematic of the thermostat setup is shown in Fig. 1a and Fig. S2. The heater acted to increase the ambient temperature within the thermostat and the temperature controller applied a temperature fluctuation to the BTO ceramic to produce a pyroelectric current. The specimen was electroded using Ag electrodes on both sides to obtain Ag/BTO/Ag device, where the as prepared poled device had a thickness and diameter of 0.65 mm and 8.7 mm, respectively; see Fig. 1b. A thermocouple was applied to the materials to

measure the temperature of the BTO based device, as seen in Fig. 1a. The probe electrodes in blue contacted with the upper and lower Ag electrodes of the device and connected with the digital source meter outside of the thermostat. A thermally insulated cover was used to limit heat exchange between the thermostat and external environment.

The phase transitions of the material were studied be measurement of the temperature-dependent volumetric specific heat capacity ($C_E$), as seen in Fig. 1c, and a permittivity-temperature ($\varepsilon_r$-$T$) curve in Fig. 2a. The polarization behavior was analyzed by measurement of the polarization-electric field hysteresis ($P$-$E$) loops.

The specific heat capacity ($C_E$) in Fig. 1c shows a small inflexion in the temperature range from room temperature to 107 ºC and begins to rise from 107 ºC, until it reaches a peak $C_E$ of ~ 3.34 J cm$^{-3}$ K$^{-1}$ at 125 ºC. It can be inferred from the $C_E$-$T$ plot that the $T_c$ of the BTO ceramic is ~ 125 ºC. The maximum value of the permittivity in $\varepsilon_r$-$T$ curve is also obtained at ~ 127 ºC, which is in good agreement with the $T_c$. The small difference of 2 ºC between the $T_c$ acquired from $C_E$-$T$ (Fig. 1c) and $\varepsilon_r$-$T$ (Fig. 2a) curves is possibly due to the different work conditions of the two test systems. The polarization-field ($P$-$E$) loops at different temperature are shown in Fig. S3, where we have selected the $P$-$E$ loops obtained at critical temperatures in Fig. 1d. The saturation polarization of the BTO based device is 15 μC cm$^{-2}$ and begins to decrease at 90 ºC. The $P$-$E$ loops are slimmer and less hysteretic at temperatures beyond 130 ºC, and the $P$-$E$ loops tend to be linear and lose their ferroelectric nature at higher temperature since the material is transforming to the paraelectric phase.

The spontaneous polarization ($P_s$) of the Ag/BTO/Ag device was obtained from the intersection point of the $y$-axis and tangent line at the top point of the $P$-$E$ loop in the first quadrant. This enabled the calculation of the spontaneous polarization of the device at different temperatures, see Fig. 2b. The

spontaneous polarization started to decrease from a temperature of 90 °C and decrease significantly on heating to 120 °C and higher, as the temperature approached $T_c$. Using Eqn. 1, it is possible to calculate $dP_s/dT$ from the differential of the $P_s$-$T$ curve to determine the pyroelectric coefficient (Equation 1); as indicated by the blue curve in Fig. 2b. The d$P_s$/d$T$-$T$ (or $p$-$T$) plot in Fig. 2b therefore indicates the dependence of $p$ with temperature. The absolute value of $p$ remained relatively stable ($p$ ~ 0.003 μC cm$^{-2}$ K$^{-1}$) from room temperature up to 80 °C and started to increase a temperature beyond 90 °C, and eventually reached a peak magnitude of $p$ ~ 0.368 μC cm$^{-2}$ K$^{-1}$ at ~ 123 °C, which is near the $T_c$ obtained from the temperature-dependent permittivity curve (Fig. 2a).

We have summarized the underlying mechanism of the pyroelectric effect at room temperature and near its $T_c$, according to the results in Fig. 1d, Fig. 2a and b. The mechanism during heating process is shown in Fig. 2c. We define that $T_0 < T_{hot} < T_0' < T_{hot}'$, $\alpha < \beta < \alpha' < \beta'$ in Fig. 2c where $T_0$ corresponds to room temperature and $T_{hot}'$ corresponds to a temperature very near to $T_c$. After being subjected to a poling process, a poled pyroelectric material has a polarization along the normal direction of electrodes marked as "$P$" in Fig. 2c. As a result of the polarization of the pyroelectric element, charges will be bound at the ends of the dipole moments, where bound charges inside the material are able to neutralize each other. However, those on the surface cannot be neutralized and to maintain surface electrical neutrality, free charges will collect on the surface to shield the bound charges (see the blue regions in Fig. 2c).

At a specific temperature the dipoles will randomly vibrate within a degree from their alignment axes and the average polarization intensity along the polarization direction is constant. As the temperature of the material is increased, the degree of vibration increases and the polarization will deviate from the alignment axes to a greater degree. As a result, the average polarization will decrease

with increasing temperature. As shown in Fig. 2c, when the temperature increases from $T_0$ to $T_{hot}$, the deviation angle increases from $\alpha$ to $\beta$, and the net polarization in normal direction decreases. As a result of the decrease in polarization, the bound charges decrease and the surface charges are now free to flow from the negative electrode to positive electrode through external circuit so that pyroelectric signals can be detected.[19, 40]

During heating above the $T_c$ the lattice structure of BTO ceramics changes from a non-centrosymmeric and ferroelectric tetragonal phase to a centrosymmetric and paraelectric cubic phase as a result of a phase transition. On the transition to a centrosymmetric paraelectric phase the spontaneous dipole moment and polarisation is reduced to zero; as in Fig. 1d.[41] Therefore, when the temperature increases from $T_0$' to $T_{hot}$' (near $T_c$), the net polarization decreases significantly due to an increase of deviation angle and a decrease of the spontaneous dipole moments. Correspondingly, as we can see in Fig. 2b, the average polarization near $T_c$ is dramatically changed and the bound charges are reduced dramatically. Accordingly, more surface screening charges are able to transfer from the negative electrode to positive electrode and larger electrical signals will be produced. And then the strengthening mechanism in cooling process is depicted in Fig. 2d. When the $T_0$" is close to $T_c$, the net polarization is fairly low. Then the temperature is cooled down to $T_{cold}$", the polarization in the normal direction of the electrodes will be rebuilt. And the corresponding surface free charges will flow in external circuit from positive electrode to negative electrode. The output current with opposite direction to that in heating process can be detected. While the $dP_s/dT$ - $T$ plot indicates the variation of the output of a pyroelectric device qualitatively, the specific output performance of the device is now measured in depth.

The pyroelectric output of the Ag/BTO/Ag device was characterized using a thermostat which

controlled the temperature. A Peltier tile was assembled in the thermostat to act as a temperature controller to produce the necessary temperature fluctuations to modulate the polarization. The temperature controller was controlled by an adjustable DC power supply and we investigated the conditions of an applied DC voltage of 1V, 3V, 5V, 7V, 9V; which corresponding to a temperature difference ($\Delta T$) of ~2 ºC, ~8.8 ºC, ~17 ºC, ~32 ºC and ~51 ºC. The DC power supply worked for 180 s and rested for 180 s in every cycle. The change rate of the DC voltage during rise and down process was kept at 3 V/s in the entire process to fix temperature change rate. The pyroelectric currents under short circuit measured at 1V, 3V, 7V, 9V are show in Fig. S5 a-d and the corresponding $T_{hot}$ (highest temperature in each cycle) can be determined from Fig. S6 a, b, d, e.

The pyroelectric response at a DC input of 5 V ($\Delta T$ ~17 ºC) were further studied due the performance enhancement and temperature stability. The corresponding temperature-time variation curve obtained at different ambient temperatures are demonstrated in Fig. 3a; it can be seen that the thermal profile is a combination of heating with periodic temperature fluctuations during heating to produce a pyroelectric response. The time of each temperature variation cycle is 360 s (heating for 180 s and resting for 180 s). The peaks and valleys temperature were defined as $T_{hot}$ and $T_{cold}$, respectively. The specific temperatures are marked on the curve, where $T_{hot}$ increased from 43.8 ºC to 137.3 ºC; see Fig. 3a. The pyroelectric current corresponding to the temperature-time curve is shown in Fig. 3b, where the peak pyroelectric current of the Ag/BTO/Ag device at $T_{hot}$ = 43.8 ºC is 10.1(4) nA and the current reached a maximum of 158.1(6) nA at $T_{hot}$ = 120.7 ºC. As a result, the peak current at $T_{hot}$ is enhanced 15.6 times by increasing the temperature to near $T_c$. We also investigated the stability of maximum pyroelectric current, where $T_{hot}$ was kept between 120.2 ºC to 121 ºC, as shown in Fig. S7a. Fig. S7b shows the pyroelectric current corresponding to the temperature-time curve, the

peak values of the current are ~145 nA without evidence of a decrease in pyroelectric response. The results indicate that the high output current near $T_c$ possesses good repeatability and stability despite being near the $T_c$. The operating temperature of piezoelectric transducers are often limited to one-half of the $T_c$ (in ºC). For the BTO material examined here this would be an upper working temperature ~ 60 ºC. While piezoelectric transducers can be subject to large electric field or mechanical stress during operation, a pyroelectric generator is subject to relatively low electric fields and stress, thereby providing potential to operation much closer to the $T_c$. [42]

The output power of the pyroelectric generator was investigated at room temperature and 120.7 ºC, where we measured the pyroelectric current with a range of load resistances and calculated the output power using $P = I^2R$. The current obtained at different load resistances are shown in Fig. S8 and the peak current versus load resistance curves at the two contrasting temperatures are shown in Fig. 3c. The peak current at the two temperatures both decreased with increasing resistance since increasing the impedance of the electrical load reduces current flow. A comparison of the output power at room temperature and 120.7 ºC is shown in Fig. 3d. The maximum output power is 122.(5) nW and 2204.(5) nW acquired at 3 GΩ and 500 MΩ at room temperature and 120.7 ºC, respectively; the output power was evidently enhanced by 18 times near $T_c$ compared to room temperature. Moreover, the output power density of the device was compared with that of other BTO based materials in Table 1. The power density obtained at 120.7 ºC in this work possesses expected advantage.[16, 43-46]

The performance figures of merit for the pyroelectric element of Ag/BTO/Ag were also investigated. The pyroelectric current can be calculated by

$$i_p = A \cdot p \cdot \frac{dT}{dt} \tag{2}$$

where $i_p$ is short circuit pyroelectric current, $A$ represents the area of the electrodes, $p$ is pyroelectric

coefficient, $T$ is temperature, $t$ is time. The equation can be converted into

$$\Delta Q_S = \int i_p dt = \int A \cdot p \cdot \frac{dT}{dt} dt = A \cdot p \cdot \Delta T \quad (3)$$

$$p = \frac{\Delta Q_s}{A \cdot \Delta T} \quad (4)$$

where $\Delta Q_s$ is the pyroelectric charge, $\Delta T$ is the temperature difference ($T_{hot}$ - $T_{cold}$).[16] The $Q_s$ of the Ag/BTO/Ag device was calculated by integrating the output current versus time curves. The $Q_s$ curves are shown in Fig. S9c and $\Delta Q_s$ is the difference between the peak and valley values of the $Q_s$ curves. Then the corresponding $p$ was determined, see Fig. 4a, where the pyroelectric coefficient increased slowly from 43.8 °C to 91.3 °C, then the rate of change in increase started to grow. The pyroelectric coefficient then increased rapidly to the maximum value at 120.7 °C and decreased as the sample was heated beyond $T_c$ and the polarization was lost. The variation with temperature is coincident with the results analyzed in Fig. 2 and the maximum value of pyroelectric coefficient $p \sim 125.(7)$ nC cm$^{-2}$ K$^{-1}$ is 5 times higher than $p \sim 24.(9)$ nC cm$^{-2}$ K$^{-1}$ at 43.8 °C. The pyroelectric coefficient of the device and other BTO based materials are listed in Table 2.[30, 37, 47-53] We also measured the performance figures of merit of the Ag/BTO/Ag device, where the pyroelectric energy conversion efficiency $\eta$ can be expressed by

$$\eta = \frac{p^2 \cdot \Delta T}{2 \cdot C_E \cdot \varepsilon_0 \cdot \varepsilon_r} \quad (5)$$

where $C_E$ represents the volumetric specific heat capacity in Fig. 1c, $\varepsilon_r$ is the relative permittivity in Fig. 2a, $\varepsilon_0$ is vacuum permittivity (8.85*10$^{-12}$ F·m$^{-1}$).[7] The figure of merit for energy harvesting ($F_E$) is

$$F_E = \frac{p^2}{\varepsilon_0 \varepsilon_r} \quad (6)$$

The figure of merit for detectivity of pyroelectric detectors ($F_d$) can be expressed as[54]

$$F_d = \frac{p}{C_E \cdot (\varepsilon_r \varepsilon_0 \tan\delta)^{0.5}} \quad (7)$$

Moreover, the figures of merit for output current and voltage are

$$F_i = \frac{p}{C_E} \quad (8)$$

$$Fv = \frac{p}{C_E \cdot \varepsilon_r \cdot \varepsilon_0} \quad (9)$$

respectively.[55] We calculated these performance figures of merit of the specimen according to the expressions above, which are summarized in Fig. 4b-f. All figures of merit possess a similar temperature variation as $p$; where $\eta$, $F_E$, $F_d$, $F_i$ and $F_v$ achieved maximum values of 0.107(4) ‰, 39.7(0) $C^2 \cdot m^{-3} \cdot K^{-2} \cdot F^{-1}$, 9.6(0)×$10^{-6}$ $C \cdot m^{3/2} \cdot J^{-1} \cdot F^{-1/2}$, 4.0(3)×$10^{-6}$ $C \cdot m \cdot J^{-1}$, 10.1(1)×$10^{-3}$ $C \cdot m^2 \cdot J^{-1} \cdot F^{-1}$ at 120.7 °C and those at 43.8 °C are 0.006(8) ‰, 2.1(2) $C^2 \cdot m^{-3} \cdot K^{-2} \cdot F^{-1}$, 2.2(2)×$10^{-6}$ $C \cdot m^{3/2} \cdot J^{-1} \cdot F^{-1/2}$, 0.8(5)×$10^{-6}$ $C \cdot m \cdot J^{-1}$, 2.8(9)×$10^{-3}$ $C \cdot m^2 \cdot J^{-1} \cdot F^{-1}$, respectively. The high performance obtained at 120.7 °C are 15.8, 18.7, 4.3, 4.7 and 3.5 times as much as those at 43.8 °C, respectively.

A temperature-dependent plot to show the peak pyroelectric current is shown in Fig. 5a. The peak current begins to increase at temperature above 81.5 °C and increase substantially from temperatures of 117 °C. On further heating, the peak current achieves a maximum of 158.1(6) nA at 120.7 °C and then begins to decrease on heating above $T_c$ where the polarization is reduced. The peak current decreased to 1.7(3) nA at 137.3 °C because the polarization along the normal direction of the electrodes decreased to zero at temperatures higher than $T_c$; this was confirmed by measurement of the piezoelectric $d_{33}$ charge coefficient, which also decreased to zero from 264 pC/N. The temperature-dependent current curve acquired at a DC voltage of 1V, 3V, 7V and 9V are shown in Fig. S10 a-d. The temperature dependence of current curve possesses a nonzero minimum value and a peak point. The features match with Lorentz function, so the current-temperature plot was fitted by Lorentz

function. The expression of Lorentz function is that

$$y = y_0 + \frac{2A}{\pi} \cdot \frac{w}{4 \cdot (x - x_c) + w^2} \tag{10}$$

Lorentz function shows a peak curve in orthogonal coordinate system. $A$ is the area of the peak, $w$ is the peak width at half height, $x_c$ is the abscissa values of the peak point, $y_0$ is the lower limit value of the curve. The obtained fitting equation is

$$I = \frac{3240.66}{(T_{hot} - 124.3)^2 + 9.24} + 13.15 \tag{11}$$

The R-square ($R^2$) of the fitting is 0.992. ($R^2$ represents the goodness of fitting, which is expected to be closed to 1). We fitted the data from 43.8 °C to 120.7 °C because the device will be depolarized after phase transition process, the fitting curve is part of a Lorentz peak curve. 124.3 is the value of the $T_{hot}$ corresponding to the peak point of the fitting curve, 13.15 is the lower limit value of $I$. The results confirmed that Ag/BTO/Ag device can work as a temperature sensor under $T_c$. The response time is defined as the time from 10 % to 90 % of the negative peak current. As shown in Fig. S11 a and b, the response time of the temperature sensor near room temperature and $T_c$ are 2.5 s and 2.8 s, respectively. In addition, Fig. 5b shows the plot of charge density and temperature change near room temperature and $T_c$. The charge density and temperature change show linear relationship near both room temperature and $T_c$. Therefore, as fabricated temperature sensor can detect temperature change. The slope of the fitting in Fig. 5b represent pyroelectric coefficient and responsivity of the sensor. The pyroelectric coefficient is consistent with the result in Fig. 4a. In addition, the responsivity of the self-powered temperature sensor near $T_c$ is 120 $nC \cdot cm^{-2} \cdot K^{-1}$, which 4.8 times higher than that near room temperature (25.1 $nC \cdot cm^{-2} \cdot K^{-1}$). Hence, the Ag/BTO/Ag temperature sensor can detect not only the temperature but also the change in temperature. And the responsivity of the sensor for temperature

change was markedly enhanced near $T_c$.

## 4. CONCLUSIONS

We designed a temperature control and detection system to investigate the pyroelectric output performance of BTO ceramic. A stable ambient temperature and temperature fluctuation were obtained and the pyroelectric output current, output power with load resistance, pyroelectric coefficient ($p$) and performance figures of merit were examined. Distinct from previous work[32, 33, 56-58], we have measured the output current and temperature fluctuation curve at different ambient temperatures directly. The pyroelectric output performance near $T_c$ was analyzed and compared with that obtained near room temperature. The pyroelectric performance was enhanced near $T_c$ and the high output performance is stable. Moreover, the phase transition properties of BTO ceramic were explored by temperature dependent volume specific heat capacity, permittivity and *P-E* loops. The *P-E* loops revealed the mechanism of the phase transition enhancement, where mechanism is that the average polarization intensity decreases dramatically near $T_c$. Since the ferroelectric-paraelectric phase transition enhancement can be extended to all ferroelectric materials with a phase transition near a useful operating temperature, it provides a route to improve the pyroelectric output performance of ferroelectric materials by controlling work temperature and designing composition and phase content. Signally, the temperature controlled output current can be applied to detect temperature. The performance of Ag/BTO/Ag temperature sensor also be enhanced by the phase transition process.

To summarize, the temperature dependent pyroelectric performance of poled Ag/BTO/Ag was measured through a thermostat and a digital source meter. The high output current and power of 158.2 nA and 2204.5 nW was obtained at $T_{hot}$ ~ 120.7 ºC near $T_c$, which were 15.6-fold and 18-fold of the counterpart at room temperature, respectively. Notably, the energy conversion efficiency was

substantially enhanced by 15.8 times. The results indicate a step forward to increase the output current and energy conversion efficiency of pyroelectric devices. Besides, the temperature sensing performance of the device was also discussed. The output current increases with temperature in Lorentz relationship. And the response time is within 3 s. The charge density change linearly increases with temperature change. So the device can detect both temperature and temperature change. The responsivity of the temperature sensor also improved 4.8 times near $T_c$. This investigation proposed and verified a method to improve the pyroelectric output performance and energy conversion efficiency of ferroelectric materials and can facilitate the practical application of pyroelectrics for self-powered temperature sensing.

## ACKNOWLEDGMENTS

This work was supported by the National Natural Science Foundation of China (Grant No. 52072041), the Beijing Natural Science Foundation (Grant No. JQ21007), and the University of Chinese Academy of Sciences (Grant No. Y8540XX2D2).

## Supporting Information

Supporting Information is available online from the Elsevier Inter Science or from the author.

## REFERENCES

[1] Y. Ji, K. Zhang, Z.L. Wang, Y. Yang, Piezo-pyro-photoelectric effects induced coupling enhancement of charge quantity in $BaTiO_3$ materials for simultaneously scavenging light and vibration energies, Energy & Environmental Science 12(4) (2019) 1231-1240.

[2] Z. Yang, S. Zhou, J. Zu, D. Inman, High-Performance Piezoelectric Energy Harvesters and Their Applications, Joule 2(4) (2018) 642-697.

[3] J. Chen, Z.L. Wang, Reviving vibration energy harvesting and self-powered sensing by a

triboelectric nanogenerator, Joule 1(3) (2017) 480-521.

[4] X. Zhao, H. Askari, J. Chen, Nanogenerators for smart cities in the era of 5G and Internet of Things, Joule 5(6) (2021) 1391-1431.

[5] C.R. Bowen, H.A. Kim, P.M. Weaver, S. Dunn, Piezoelectric and ferroelectric materials and structures for energy harvesting applications, Energy & Environmental Science 7(1) (2014) 25-44.

[6] C.R. Bowen, J. Taylor, E. LeBoulbar, D. Zabek, A. Chauhan, R. Vaish, Pyroelectric materials and devices for energy harvesting applications, Energy & Environmental Science 7(12) (2014) 3836-3856.

[7] H. Li, C.R. Bowen, Y. Yang, Scavenging Energy Sources Using Ferroelectric Materials, Advanced Functional Materials 31(25) (2021) 23.

[8] K. Song, R. Zhao, Z. Wang, Y. Yang, Conjuncted Pyro-Piezoelectric Effect for Self-Powered Simultaneous Temperature and Pressure Sensing, Advanced Materials 31(36) (2019) e1902831.

[9] J. Ma, Y. Zhang, Y. Liu, D. Han, J. Mao, J. Zhang, W. Zhao, H. Sun, Heterogeneous self-healing assembly of MXene and graphene oxide enables producing free-standing and self-reparable soft electronics and robots, Science Bulletin 67(5) (2021) 501-511.

[10] F. Zhong, W. Hu, P. Zhu, H. Wang, C. Ma, N. Lin, Z. Wang, Piezoresistive design for electronic skin: from fundamental to emerging applications, Opto-Electronic Advances 5(0) (2020) 210029.

[11] H.i.P. Association, About Waste Heat. <https://www.heatispower.org/waste-heat/>, 2021.

[12] X. Shi, J. Zou, Z. Chen, Advanced Thermoelectric Design: From Materials and Structures to Devices, Chemical Reviews 120(15) (2020) 7399-7515.

[13] B. Qin, D. Wang, X. Liu, Y. Qin, J.-F. Dong, J. Luo, J.-W. Li, W. Liu, G. Tan, X. Tang, J.-F. Li, J. He, L.-D. Zhao, Power generation and thermoelectric cooling enabled by momentum and energy multiband alignments, Science 373(6554) (2021) 556-561.

[14] W. Chen, X. Shi, J. Zou, Z. Chen, Wearable fiber-based thermoelectrics from materials to applications, Nano Energy 81 (2021) 105684.

[15] W. Liu, L. Yang, Z. Chen, J. Zou, Promising and Eco-Friendly $Cu_2X$-Based Thermoelectric Materials: Progress and Applications, Advanced Materials 32(8) (2020) 1905703.

[16] K. Song, N. Ma, Y.K. Mishra, R. Adelung, Y. Yang, Achieving Light-Induced Ultrahigh Pyroelectric Charge Density Toward Self-Powered UV Light Detection, Advanced Electronic Materials 5(1) (2019) 1800413.

[17] Y. Yang, W. Guo, K.C. Pradel, G. Zhu, Y. Zhou, Y. Zhang, Y. Hu, L. Lin, Z.L. Wang, Pyroelectric Nanogenerators for Harvesting Thermoelectric Energy, Nano Letters 12(6) (2012) 2833-2838.

[18] Y. Yang, S. Wang, Y. Zhang, Z.L. Wang, Pyroelectric Nanogenerators for Driving Wireless Sensors, Nano Letters 12(12) (2012) 6408-6413.

[19] Y. Yang, J.H. Jung, B.K. Yun, F. Zhang, K.C. Pradel, W. Guo, Z.L. Wang, Flexible Pyroelectric Nanogenerators using a Composite Structure of Lead-Free $KNbO_3$ Nanowires, Advanced Materials 24(39) (2012) 5357-5362.

[20] H. Xue, Q. Yang, D. Wang, W. Luo, W. Wang, M. Lin, D. Liang, Q. Luo, A wearable pyroelectric nanogenerator and self-powered breathing sensor, Nano Energy 38 (2017) 147-154.

[21] H. Athenstaedt, H. Claussen, D. Schaper, Epidermis of Human Skin: Pyroelectric and Piezoelectric Sensor Layer, Science 216(4549) (1982) 1018-1020.

[22] J.H. Lee, K.Y. Lee, M.K. Gupta, T.Y. Kim, D.Y. Lee, J. Oh, C. Ryu, W.J. Yoo, C.Y. Kang, S.J. Yoon, J.B. Yoo, S.W. Kim, Highly Stretchable Piezoelectric-Pyroelectric Hybrid Nanogenerator, Advanced Materials 26(5) (2014) 765-769.

[23] J. Yan, P. Lou, R. Li, J. Hu, J. Xiong, Research on the Multiple Factors Influencing Human

Identification Based on Pyroelectric Infrared Sensors, Sensors 18(2) (2018) 604.

[24] K. Mistewicz, Pyroelectric nanogenerator Based on an SbSI-$TiO_2$ nanocomposite, Sensors 22(1) (2021) 69.

[25] K. Mistewicz, M. Jesionek, M. Nowak, M. Kozioł, SbSeI pyroelectric nanogenerator for a low temperature waste heat recovery, Nano Energy 64 (2019) 103906.

[26] C. Li, S. Xu, J. Yu, Z. Li, W. Li, J. Wang, A. Liu, B. Man, S. Yang, C. Zhang, Local hot charge density regulation: Vibration-free pyroelectric nanogenerator for effectively enhancing catalysis and in-situ surface enhanced Raman scattering monitoring, Nano Energy 81 (2021) 105585.

[27] F. Narita, M. Fox, K. Mori, H. Takeuchi, T. Kobayashi, K. Omote, Potential of energy harvesting in barium titanate based laminates from room temperature to cryogenic/high temperatures: measurements and linking phase field and finite element simulations, Smart Materials and Structures 26(11) (2017) 115027.

[28] J. Kim, J.H. Lee, H. Ryu, J.-H. Lee, U. Khan, H. Kim, S.S. Kwak, S.-W. Kim, High-performance piezoelectric, pyroelectric, and triboelectric nanogenerators based on P(VDF-TrFE) with controlled crystallinity and dipole alignment, Advanced Functional Materials 27(22) (2017) 1700702.

[29] S. Pandya, J. Wilbur, J. Kim, R. Gao, A. Dasgupta, C. Dames, L.W. Martin, Pyroelectric energy conversion with large energy and power density in relaxor ferroelectric thin films, Nature Materials 17(5) (2018) 432-438.

[30] S. Patel, M. Kumar, Influence of grain size on the electrocaloric and pyroelectric properties in non-reducible $BaTiO_3$ ceramics, AIP Advances 10(8) (2020) 085302.

[31] Y. Yang, Y. Zhou, J.M. Wu, Z.L. Wang, Single Micro/Nanowire Pyroelectric Nanogenerators as Self-Powered Temperature Sensors, ACS Nano 6(9) (2012) 8456-8461.

[32] Z. Sun, Y. Tang, S. Zhang, C. Ji, T. Chen, J. Luo, Ultrahigh Pyroelectric Figures of Merit Associated with Distinct Bistable Dielectric Phase Transition in a New Molecular Compound: Di-n-Butylaminium Trifluoroacetate, Advanced Materials 27(32) (2015) 4795-4801.

[33] S. Li, H. Nie, G. Wang, N. Liu, M. Zhou, F. Cao, X. Dong, Novel $AgNbO_3$-based lead-free ceramics featuring excellent pyroelectric properties for infrared detecting and energy-harvesting applications via antiferroelectric/ferroelectric phase-boundary design, Journal of Materials Chemistry C 7(15) (2019) 4403-4414.

[34] B. Jiang, J. Iocozzia, L. Zhao, H. Zhang, Y.-W. Harn, Y. Chen, Z. Lin, Barium titanate at the nanoscale: controlled synthesis and dielectric and ferroelectric properties, Chemical Society Reviews 48(4) (2019) 1194-1228.

[35] Y. Zhao, X.Q. Liu, S.Y. Wu, X.M. Chen, Effect of phase transition on electrocaloric effect in Indium substituted $BaTiO_3$ ceramics, Journal of Alloys and Compounds 822 (2020) 153632.

[36] A. Thakre, D. Maurya, D.Y. Kim, Y. Kim, P. Sriboriboon, I.-R. Yoo, S. Priya, K.-H. Cho, H.-C. Song, J. Ryu, Enhanced pyroelectric response from domain-engineered lead-free $(K_{0.5}Bi_{0.5}TiO_3$-$BaTiO_3)$-$Na_{0.5}Bi_{0.5}TiO_3$ ferroelectric ceramics, Journal of the European Ceramic Society 41(4) (2021) 2524-2532.

[37] L. Li, S. Wang, X. Li, Y. Sha, Z. Liu, L. Liu, J. Zhang, S.T. Zhang, Y. Wang, Large pyroelectricity via engineered ferroelectric‐relaxor phase boundary, Journal of the American Ceramic Society 105(8) (2022) 5230-5239.

[38] X.H. Wang, X.Y. Deng, H.L. Bai, H. Zhou, W.G. Qu, L.T. Li, I.W. Chen, Two-step sintering of ceramics with constant grain-size, II: $BaTiO_3$ and Ni-Cu-Zn Ferrite, Journal of the American Ceramic Society 89(2) (2006) 438-443.

[39] I.W. Chen, X. Wang, Sintering dense nanocrystalline ceramics without final-stage grain growth, Nature 404 (2000) 168-171.

[40] S.B. Lang, Pyroelectricity: From ancient curiosity to modern imaging tool, Physics Today 58(8) (2005) 31-36.

[41] N. Funsueb, A. Limpichaipanit, A. Ngamjarurojana, Electrical properties and microstructure of phase combination in $BaTiO_3$-based Ceramics, Journal of Physics: Conference Series 1144 (2018) 012133.

[42] J. Chen, X.L. Tan, W. Jo, J. Rodel, Temperature dependence of piezoelectric properties of high-T-C $Bi(Mg_{1/2}Ti_{1/2})O_3$-$PbTiO_3$, Journal of Applied Physics 106(3) (2009) 7.

[43] N. Ma, Y. Yang, Enhanced self-powered UV photoresponse of ferroelectric $BaTiO_3$ materials by pyroelectric effect, Nano Energy 40 (2017) 352-359.

[44] N. Ma, K. Zhang, Y. Yang, Photovoltaic-pyroelectric coupled effect induced electricity for self-powered photodetector system, Advanced Materials 29(46) (2017) 1703694.

[45] Y. Ji, Y. Wang, Y. Yang, Photovoltaic-pyroelectric-piezoelectric coupled effect induced electricity for self‐powered coupled sensing, Advanced Electronic Materials 5(6) (2019) 1900195.

[46] R.M. Raghavendra, K.P.S.S. Praneeth, S. Dutta, Preparation and characterization of $BaTiO_3$-$PbZrTiO_3$ coating for pyroelectric energy harvesting, Journal of Electronic Materials 46(1) (2016) 101-106.

[47] K. Srikanth, S. Patel, R. Vaish, Pyroelectric performance of $BaTi_{1-x}Sn_xO_3$ ceramics, International Journal of Applied Ceramic Technology 15(2) (2018) 546-553.

[48] M. Aggarwal, M. Kumar, R. Syal, V.P. Singh, A.K. Singh, S. Dhiman, S. Kumar, Enhanced pyroelectric figure of merits in Sr and Zr co-doped porous $BaTiO_3$ ceramics, Journal of Materials

Science: Materials in Electronics 31(3) (2020) 2337-2346.

[49] S. Zeng, X. Tang, Q. Liu, Y. Jiang, M. Li, W. Li, Z. Tang, Electrocaloric effect and pyroelectric properties in Ce-doped $BaCe_xTi_{1-x}O_3$ ceramics, Journal of Alloys and Compounds 776 (2019) 731-739.

[50] C.H. Liow, X. Lu, K. Zeng, S. Li, G.W. Ho, Optically Governed Dynamic Surface Charge Redistribution of Hybrid Plasmo-Pyroelectric Nanosystems, Small 15(36) (2019) e1903042.

[51] P.K. Singh, M.S. Gaur, D. Johari, R. Sagar, A. Gupta, A. Sharma, G. Singh, M. Yadav, Enhanced pyroelectric and piezoelectric properties of PVDF-$BaTiO_3$ nanocomposites layered samples, Ferroelectrics 551(1) (2019) 122-132.

[52] J. Jia, S. Guo, S. Yan, F. Cao, C. Yao, X. Dong, G. Wang, Simultaneous large pyroelectric response and high depolarization temperature in sodium bismuth titanate-based perovskites, Applied Physics Letters 114(3) (2019) 032902.

[53] K. Zhao, B. Ouyang, Y. Yang, Enhancing photocurrent of radially polarized ferroelectric $BaTiO_3$ materials by ferro-pyro-phototronic effect, iScience 3 (2018) 208-216.

[54] R.W. Whatmore, Pyroelectric devices and materials, Reports on Progress in Physics 49(12) (1986) 1335-1386.

[55] Y. Zhang, M. Xie, J. Roscow, Y. Bao, K. Zhou, D. Zhang, C.R. Bowen, Enhanced pyroelectric and piezoelectric properties of PZT with aligned porosity for energy harvesting applications, Journal of Materials Chemistry A 5(14) (2017) 6569-6580.

[56] F. Guo, B. Yang, S. Zhang, F. Wu, D. Liu, P. Hu, Y. Sun, D. Wang, W. Cao, Enhanced pyroelectric property in $(1-x)(Bi_{0.5}Na_{0.5})TiO_3$-$xBa(Zr_{0.055}Ti_{0.945})O_3$: Role of morphotropic phase boundary and ferroelectric-antiferroelectric phase transition, Applied Physics Letters 103(18) (2013) 182906.

[57] C.B. Richard A. Whiter, Michael Smith, and SohiniKar-Narayan, Mechanical Energy Harvesting Performance of FerroelectricPolymer Nanowires Grown via Template Wetting, Energy Technology 6(5) (2018) 928 –934.

[58] P. Qiao, Y. Zhang, X. Chen, M. Zhou, G. Wang, X. Dong, Enhancing pyroelectric properties in $(Pb_{1-1.5x}La_x)(Zr_{0.86}Ti_{0.14})O_3$ ceramics through composition modulated phase transition, Ceramics International 45(6) (2019) 7114-7119.

# FIGURES

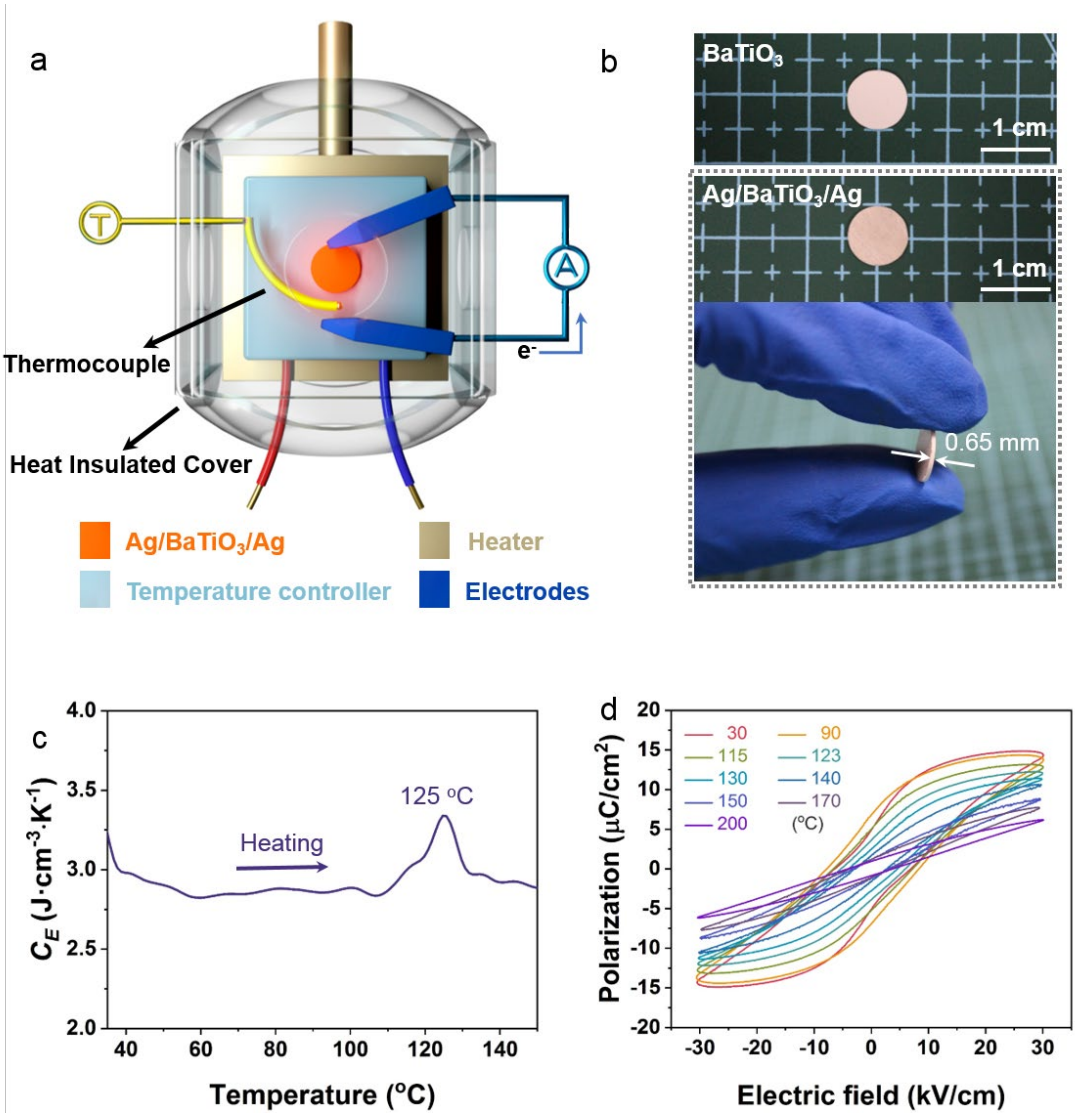


**Figure 1.** (a) Schematic of measurement system (front view). (b) Images of BTO ceramic and Ag/BTO/Ag device. (c) Temperature-dependent volumetric specific heat capacity of Ag/BTO/Ag device. (d) Polarization-electric field hysteresis loops of Ag/BTO/Ag device with temperature.

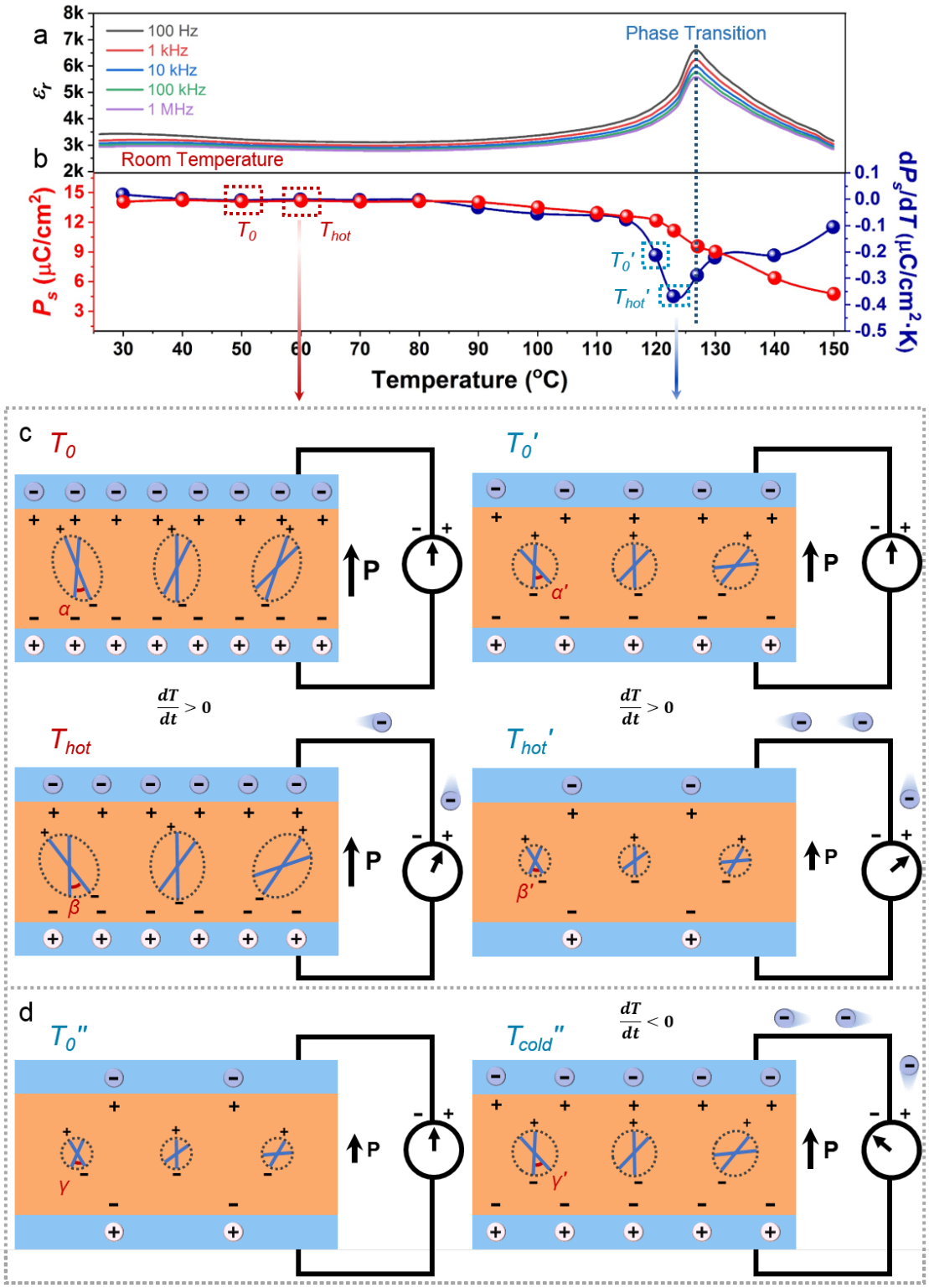


**Figure 2.** Mechanism and analysis of the pyroelectric effect enhancement near the $T_c$. (a) Temperature-dependent permittivity curve. (b) Temperature-dependent polarization and the polarization gradient with temperature curves. (c) Comparison of the physical mechanism of the pyroelectric performance near room temperature and $T_c$ in heating process, which reveal the enhancement mechanism. (d) Physical mechanism of the pyroelectric performance near $T_c$ in cooling process.

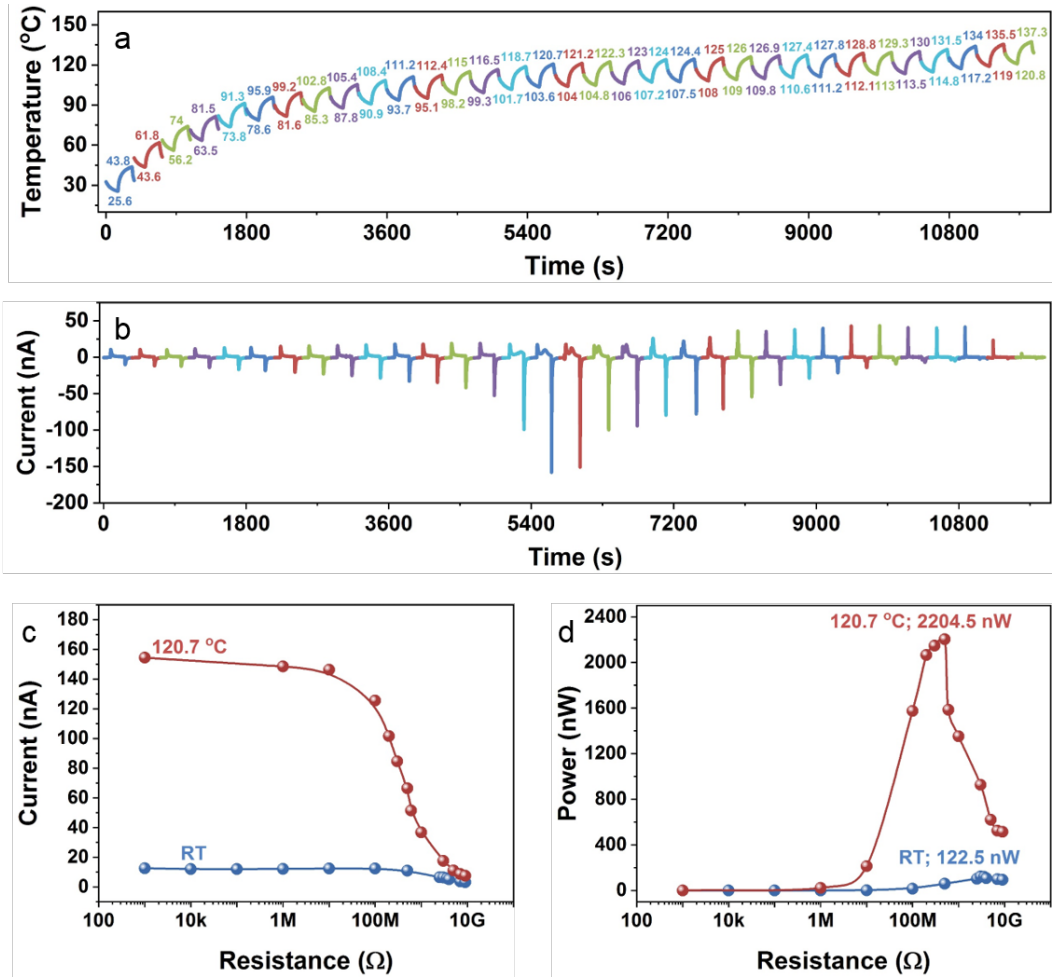


**Figure 3.** Pyroelectric current from 43.8 °C ~ 137.3 °C. **(**a) Temperature-time variation curve. (b) Output current variation with time corresponding to the temperature-time curve in Figure 2a. (c, d) Output current and corresponding output power at different loading resistance near room temperature and $T_c$.

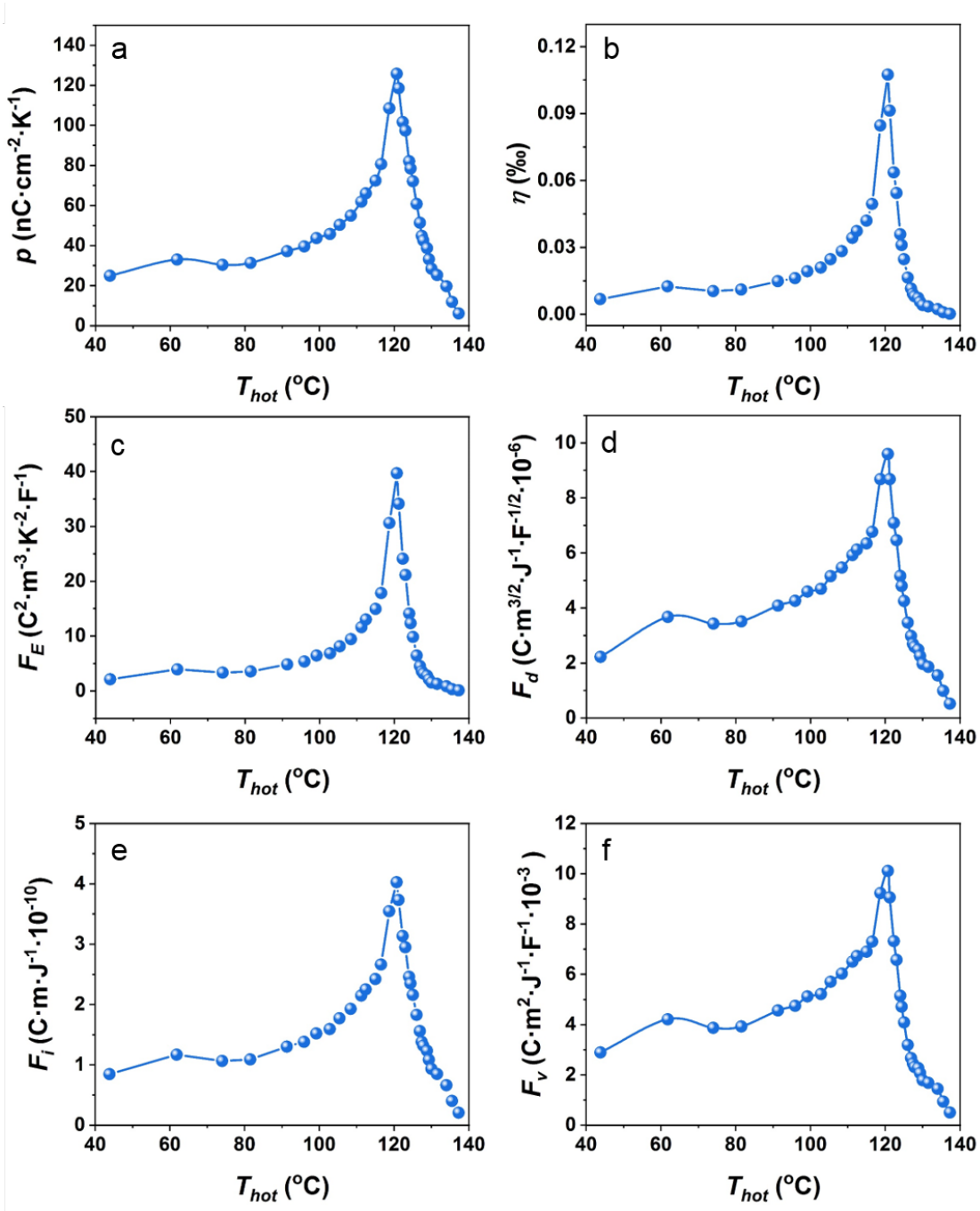


**Figure 4.** Performance figures of merit of Ag/BTO/Ag with a temperature difference of 17 °C. Curves of (a) pyroelectric coefficient (b) energy conversion efficiency (c) figure of merit for energy harvesting (d) figure of merit for pyroelectric detectivity (e) figure of merit for current, (f) figure of merit for voltage versus $T_{hot}$.

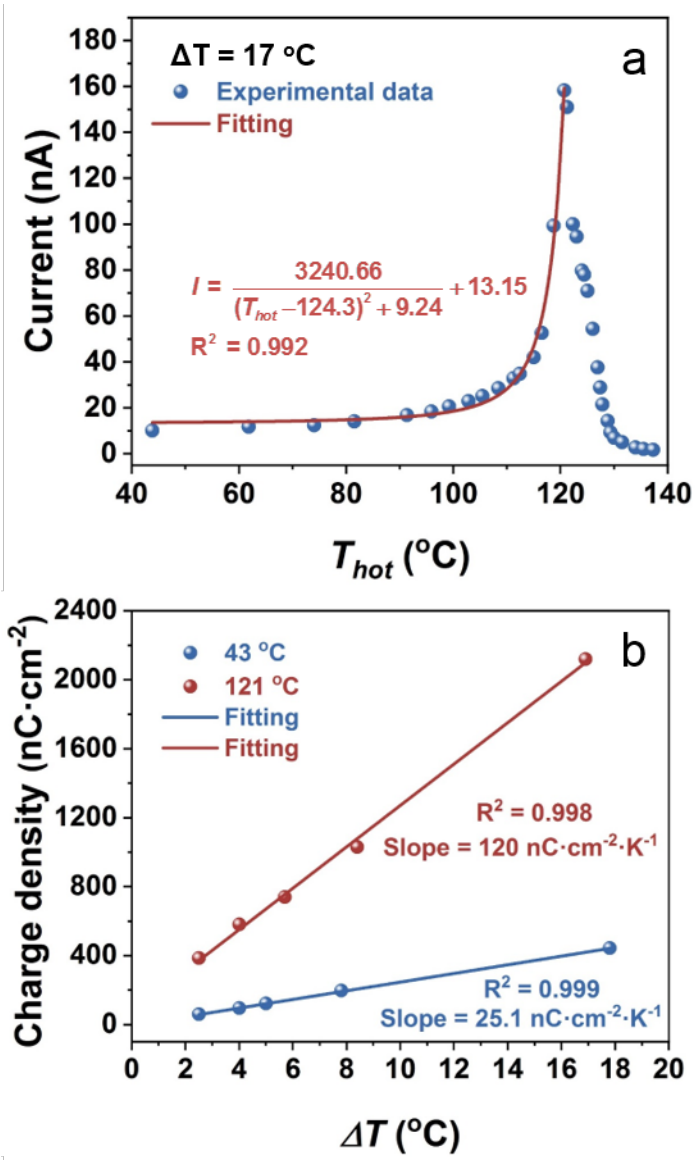


**Figure 5.** (a) The variation of the peak current with $T_{hot}$. (b) Dependence of charge density on temperature difference ($\Delta T$).

**Table 1.** Comparison of the output power of BTO based materials.

| Composition | Power density ($nW/cm^2$) | Loading Resistance (MΩ) | Temperature (°C) | $\Delta T$ (°C) | Reference |
|---|---|---|---|---|---|
| BTO | 219.9 | 500 | 120.7 | 17 | This Work |
| BTO | 3957.8 | 1000 | 43.8 | 17 | This Work |
| BTO | 11.9 | 1000 | RT | 12.4 | 43 |
| BTO | 51.2 | 40 | RT | 11.3 | 44 |
| BTO | 12.4 | 750 | RT | 12.9 | 45 |
| BTO | 639.2 | 100 | RT | 44.2 | 16 |
| 0.5BTO-0.5PZT | 130 | -- | 154 ($T_c$) | -- | 46 |

$\Delta T$ is temperature difference; PZT is $PbZr_{0.52}Ti_{0.48}O_3$

**Table 2.** Comparison of the pyroelectric coefficient of BTO based materials.

| Composition | Pyroelectric coefficient ($nC/cm^2 \cdot K$) | Temperature (°C) | Reference |
|---|---|---|---|
| BTO | 125.7 | 120.7 | This Work |
| BTO | 24.9 | 43.8 | This Work |
| 0.85PNZST-0.15BTO | 113 | RT | 37 |
| $BaTi_{0.95}Sn_{0.05}O_3$ | 100 | RT | 47 |
| $Ba_{0.85}Sr_{0.15}Zr_{0.1}Ti_{0.9}O_3$ | 80.5 | RT | 48 |
| $BaCe_{0.1}Ti_{0.9}O_3$ | 78.2 | RT | 49 |
| BTO-Ag nanosystem | 33.5 | 77 | 50 |
| PVDF 7wt.%-BTO | 26.85 | 130 | 51 |
| $0.8Bi_{0.5}Na_{0.5}TiO_3$-$0.2BaTiO_3$ | 24.2 | RT | 52 |
| BTO sintering from nanowire | 16 | RT | 53 |
| BTO | 10 | RT | 30 |

RT is room temperature; BTO is $BaTiO_3$; PNZST is $Pb_{0.99}Nb_{0.02}[(Zr_{0.57}Sn_{0.43})_{0.937}Ti_{0.063}]_{0.98}O_3$

**Hongyu Li** is currently a doctoral candidate in the research group of Prof. Ya Yang at Beijing Institute of Nanoenergy and Nanosystems, Chinese Academy of Sciences (CAS). Her research interest focus on pyroelectric nanogenerator and and ferroelectric material.

**Prof. Chris R. Bowen** has a BSc degree in Materials Science from the University of Bath (1986-1990) and a DPhil from the University of Oxford (1990-1993). Post-doctoral work was at Tecnische Universita¨t Harburg-Hamburg and University of Leeds (1994-1996). He was Senior Scientist at the Defence Evaluation and Research Agency from 1996-1998. He joined University of Bath as a Lecturer in 1998 and is now Professor of Materials. Research includes energy harvesting, ferroelectrics and functional ceramics.

**Prof. Ya Yang** received his Ph.D. in Materials Science and Engineering from University of Science and Technology Beijing, China. He is currently a professor at Beijing Institute of Nanoenergy and Nanosystems, Chinese Academy of Sciences, China. His main research interests focus on ferroelectric materials and devices for energy conver-sion, self-powered sensing, and some new physical effects. He has published one book and more than 190 SCI academic papers in Science Advances and other journals. These papers have been cited by more than 16000 times, and the corresponding H-index is 75. He is the Editor-in-Chief of Nanoenergy Advances and is the editorial committee member of InfoMat, Nano-Micro Letters, Nanoscale, iScience, Nanoscale Advances, and some other journals. He is the Guest Editor of Research, iScience, Nanomaterials, and Energies. Details can be found at: http://www.researcherid.com/rid/A-7219-2016.